The human ventromedial prefrontal cortex sulcal morphology and its influence on its functional organization.

Alizée LOPEZ-PERSEM[1*], Lennart VERHAGEN[1], Céline AMIEZ[2], Michael PETRIDES[3], Jérome SALLET[1*].

1. Wellcome Integrative Neuroimaging Centre, Department of Experiemental Psychology, University of Oxford, Oxford OX1 3SR, United Kingdom
2. Univ Lyon, Université Lyon 1, Inserm, Stem Cell and Brain Research Institute U1208, 18, Avenue du Doyen Lépine, 69500 Bron, France
3. Montreal Neurological Institute, McGill University, Montreal, QC H3A2B4, Canada

Abreviated title: **vmPFC morphology and functional organization**

*Corresponding Authors:

- Alizée Lopez-Persem, lopez.alizee@gmail.com
- Jerome Sallet, Jerome.sallet@psy.ox.ac.uk

ABSTRACT

The ventromedial prefrontal cortex (vmPFC) is a key brain region supporting decision-making processes and it has been shown to be one of the main hubs of the Default Mode Network, a network classically activated during resting state. However, the anatomy of the 'vmPFC' that comprises several distinct cytoarchitectonic areas, is not well characterized. We studied here the important inter-individual variability of the vmPFC sulcal morphology and found that the presence/absence of the inferior rostral sulcus and the subgenual intralimbic sulcus influences significantly the sulcal organization of the vmPFC. Furthermore, the sulcal organization influences the location of the vmPFC peak of the Default Mode Network, demonstrating that the location of functional activity can be affected by local sulcal patterns. These results are critical for the investigation of the function of the vmPFC and show that taking into account the sulcal variability might be essential to guide the interpretation of neuroimaging studies.

SIGNIFICANT STATEMENT

The ventromedial prefrontal cortex (vmPFC) is one of the main hub of the Default Mode Network. However, the term 'vmPFC' does not refer to a specific anatomical delineated brain area. Instead, it refers to a large portion of the prefrontal cortex. In our study, we provide a complete description of the inter-individual

variability of the vmPFC morphology. We showed that two supplementary medial sulci affect the most the organization of the vmPFC, which in turn affect the location of the functional peak of activity in this region. Those results show that taking into account the variability in sulcal patterns might be essential to guide the interpretation of neuroimaging studies of the vmPFC.

INTRODUCTION

Making adaptive decisions in a changing environment relies to a significant extent on our ability to evaluate and learn the values associated with the possible options that we are facing. There is considerable evidence that the ventromedial prefrontal cortex (vmPFC) is a key region for such processes (Lebreton et al., 2009; Lopez-Persem et al., 2016; Noonan et al., 2010).

However, this brain region is not only involved in reward and value processing but also in emotional regulation (Hänsel and von Känel, 2008), memory representation (Bonnici et al., 2012) and it is a main hub of the Default Mode Network (Raichle, 2015), a network classically observed during resting-state and mind-wandering. Therefore, the vmPFC function is the focus of many studies of a wide variety of cognitive processes.

Defining the functional contributions of a cortical territory requires first an understanding of its anatomical organization. The distinct cytoarchitectonic areas found in a region have been shown to have distinct connectivity with other cortical and subcortical areas and also to relate to distinct functional processes (Petrides, 2002;

Petrides and Baddeley, 1996). These cytoarchitectonic areas often relate to sulcal patterns that can be clearly visualized in functional imaging studies. Indeed, the functional contributions of brain areas are constrained by their inputs and outputs, i.e. their connectivity patterns (Passingham et al., 2002; Petrides, 2002). Characterizing the functions of the vmPFC is notably challenging for two reasons. First, the term 'vmPFC' does not refer to a specific anatomically delineated brain area. In functional neuroimaging studies that are based on the average brain activity of a group have used the term 'vmPFC' to label a large portion of the prefrontal cortex (Bartra et al., 2013) that includes several cytoarchitectonic areas 10, 14, 25 and 32 (Figure 1) and vmPFC boundaries are debated (Wallis, 2011). The second challenge in assigning a function to the different subdivisions of the vmPFC comes from the fact that the classic neuroimaging approach is to average results across subjects in the Montreal Neurological Institute (MNI) stereotactic space (Evans et al., 1993). This method therefore ignores the considerable interindividual variability of the morphological sulcal patterns of the vmPFC (Chiavaras and Petrides, 2000; Mackey and Petrides, 2014). It should be emphasized here that there is evidence in the vmPFC that cytoarchitectonic areas relate well to particular sulci (Mackey and Petrides, 2014).

Sulcal patterns could indeed vary either in terms of presence / absence or in terms of shape / relative position of sulci. Importantly, it has been shown that the locations of distinct experienced value signals could be predicted from the organization of the OFC sulci (Li et al., 2015). Moreover, taking into account the variability in sulcal patterns has proven to be essential to guide the interpretation of neuroimaging studies

in the lateral prefrontal cortex and the cingulate cortex (Amiez, 2006; Amiez et al., 2013). Thus, differences in functional properties in the vmPFC could also be related to the morphological heterogeneity across individuals.

In the present study, we first provide a precise description of the sulci of the vmPFC, then, we show that distinct morphological patterns exist among individuals and how those patterns affect the sulcal organization of the vmPFC. Finally, we show that this information is relevant to the study of the function of the vmPFC through a link between sulcal anatomy and the local response of the Default Mode Network.

MATERIALS AND METHODS

Subjects

The data used in this study belongs to the Human Connectome Project (https://db.humanconnectome.org) (Van Essen et al., 2012). We selected the S900 subjects release with 7T structural and resting-state fMRI data. The data were preprocessed according to the HCP pipeline (Glasser et al., 2013). All analyses were conducted on the data aligned using areal-feature-based registration (called "MSMAll" for "Multimodal Surface Matching" (Glasser et al., 2016)). Out of the 73 subjects of this specific HCP release, 16 subjects were excluded because of family ties with other subjects of the database. The data analysis was therefore based on 114 hemispheres of 57 subjects (37 females).

Sulcal identification

The analyses were restricted to the ventral part of the medial wall of the prefrontal cortex, delineated by an arbitrary horizontal line that runs from the front of the brain to the genu of the corpus callosum. Following (Mackey and Petrides, 2014), we identified two main sulci that we labelled suprarostral sulcus (SU-ROS) and superior rostral sulcus (ROS-S). An additional sulcus, ventral to the ROS-S, was observed in several subjects, labelled as the inferior rostral sulcus (ROS-I).

Fronto-polar sulci, identified as MPS (medial polar sulci) in (Mackey and Petrides, 2014), were dissociated in three potentials sulci: ASOS (accessory supra-orbital sulcus), MPS (medial polar sulci) and SOS (supra-orbital sulcus). We distinguished them as follows: the MPS is formed by a fold in the fronto-polar cortex creating a sulcus on the medial wall while ASOS and SOS were defined as a fold on the medial wall itself. SOS was in general more dorsal than ASOS and PMS. An additional Ventromedial Polar Sulcus (VMPS) was identified. The VMPS has the singularity to be directed toward the orbital part of the cortex and lies dorsally to the olfactory sulcus.

Although the cingulate cortex was not the focus of the present study, the cingulate sulci were also identified because they are necessary to define the morphological patterns of the ventromedial sulci. The main cingulate sulcus (CGS) was identified in all subjects, but the para-cingulate sulcus (PCGS), a secondary sulcus, was sometimes observed either as a well-marked sulcus or as a trace of it, that we labelled as spur-PCGS. Finally we identify the SILS (subgenual intralimbic sulcus). It has the

characteristic to be subgenual and located between the SU-ROS and the corpus callosum.

The cortical surface renderings were generated using the Connectome Workbench display tool (http://www.humanconnectome.org/connectome/connectome-workbench.html) (Marcus et al., 2011). In order to assign properly a label on each sulcus observed in every hemisphere, we examined three types of renderings of the medial wall: the volume (T1), the midthickness surface and the dilated surface with a projection of the curvature (Figure 1). We then manually drew the sulcus on the dilated surface following the curvature projection.

Morphological analysis

All analyses and statistics were conducted in Matlab 2017a (MATLAB and Statistics Toolbox Release 2017a, The MathWorks, Inc., Natick, Massachusetts, United States) with home functions calling Workbench functions. To compute the statistics and get information on each type of sulcus, regions of interest were created from the manual drawing explained above for every hemisphere. MNI coordinates were accessible in all the surface files provided in the HCP dataset. For display purposes, in the Figure 4E, we used a dilated version of the sulci (5mm larger) for the analysis on the normalized length in order to increase the number of points entered in the analysis. The results were, however, did not change when the original sulcus was used as a region of interest (posterior versus anterior part weight comparison: $t(113)=-3.98$, $p=1.10^{-4}$).

To compute the probability of observing one sulcus on one side given its presence on the other side, we used the following equation:

$$P(S_B|S_1) = \frac{P(S_1|S_B) * P(S_B)}{P(S_1)} = \frac{P(S_B)}{P(S_1)}$$

With $P(S_B)$ the probability of sulcus on both sides, $P(S_1)$ the probability of sulcus on only one side. $P(S_1|S_B)=1$.

Resting state analysis

The rs-fMRI acquisitions (including the use of leading-edge, customized MRI hardware and acquisition software) and image processing are covered in detail in (Glasser et al., 2013; Smith et al., 2013; Uğurbil et al., 2013). Following image preprocessing (primarily using the FMRIB Software Library [FSL] (Jenkinson et al., 2012), FreeSurfer (Fischl, 2012), and Connectome Workbench (Marcus et al., 2013) software packages), the HCP applies data-driven artefact removal to rs-fMRI time series. First, ICA is applied to each 15-min rs-fMRI dataset separately to identify both structured artefact and non-artefact components. These components are then automatically classified into artefact ('noise') versus non-artefact ('signal'), using machine learning – a hand-trained hierarchical classifier (FMRIB's ICA-based X-noisifier [FIX]) (Smith et al., 2013). Each signal component corresponds to a specific brain network. To identify the component capturing the Default Mode Network, we examined them one by one for every subject and extracted the selected component.

RESULTS

Description of the sulci

Using a subset of 57 subjects (i.e. 114 hemispheres) from the Human Connectome Project (see Methods), we identified all the possible sulci within the left and right hemispheres of the ventral part of the medial wall of the Prefrontal Cortex, i.e. the ventro-medial Prefrontal Cortex (vmPFC). Three categories of sulci were observed: the principal medial sulci, the supplementary medial sulci and the polar/supra-orbital sulci. We provide in the following part a description of those sulci (Figure 1 and Table 1).

Principal medial sulci

The supra-rostral sulcus (SU-ROS) and the superior rostral sulcus (ROS-S) were identified in all hemispheres. The mean average length of the SU-ROS was 36.87±0.73 mm with no significant difference between the left and right hemispheres (left: 36.71±0.94 mm, right: 37.03±1.13 mm; left vs right: $t(112)=-0.21$, $p=0.83$). The ROS-S had an average length of 28.78±0.95 mm with a significant difference between the left and right hemispheres (left: ROS-S is 25.29±1.46 mm, right: 32.27±1.02 mm; left vs right: $t(112)=-3.92$, $p=2.10^{-4}$). We did not find any significant correlation between the length of the sulci on the two hemispheres across subjects (SU-ROS: $r=-0.13$, $p=0.35$, ROS-S: $r=0.20$, $p=0.13$).

At the group level, we observed an overlap in the MNI locations of the centre of gravity of those two sulci. The ROS-S average location was y=48.20(±0.61), z=-15.84 (±0.34) on the left side and y=46.68 (±0.49), z=--14.84 (±0.29) on the right side, and the SU-ROS average location was y=44.86 (±0.42), z=-8.78 (±0.46) on the left side and y=44.37 (±0.37), z=-6.45 (±0.32) on the right side. However, on the dorso-ventral axis, the range of location of the ROS-S on the left side varied from z=-21 to -9 mm and from z=-16 to 4 mm for the SU-ROS, indicating that, at the group level, there is an overlap in the MNI coordinates of these two sulci, notably between z=-16 and -9 mm. This result was also observed in the right hemisphere with a ROS-S range from z=-20 to -7 mm and a SU-ROS range from z=-12 to 0 mm.

Supplementary medial sulci

The inferior rostral sulcus (ROS-I) was present in 64.04% of the hemispheres, with 52.63% and 75.44% in the left and right hemispheres, respectively. The ROS-I was significantly more frequent in the right hemisphere compared with the left hemisphere ($t(112)=-2.59$, $p=0.01$). The ROS-I average location was y=54.60(±0.40), z=-17.18(±0.28) on the left side and y=54.67(±0.53), z=-17.23(±0.26) on the right side. The probability of having an ROS-I on both sides given its presence on one side or the other was estimated at 52.08%, suggesting a relative independence of the two hemispheres regarding this sulcus.

The length of the ROS-I was on average 12.74±0.70 mm with no difference between the two hemispheres (left: 13.04±1.07 mm; right: 12.54±0.93 mm; left vs right: $t(71)=0.35$,

p=0.72). There was no correlation of length between the two hemispheres when it was present on both sides (r=0.11, p=0.59).

The subgenual intralimbic sulcus (SILS) was identified in 43.86% of the hemispheres, with 64.91% and 22.81% of the left and right hemispheres, respectively. The difference between hemispheres was significant (t(112)=4.96, $p=3.10^{-6}$), i.e. it was more probable to find this sulcus in only one hemisphere compared to the two hemispheres (the probability that SILS is on both sides given its presence on one side was 19.05%). The SILS average location was y=39.09(±0.45), z=-3.19(±0.82) on the left side and y=38.34(±0.38), z=-0.48(±1.06) on the right side. With an average length of 27.93±1.13 mm, there was no significant difference of the SILS length between the two hemispheres (t(48)=-1.51, p=0.14) and no correlation of length for the cases in which SILS was found in both hemisphere (r=0.27, p=0.52)

Polar and supra-orbital sulci

The polar supra-orbital sulcus (SOS) was found in all hemispheres. The accessory supra-orbital sulcus (ASOS) was present in 93.86% of the hemispheres with no over representation in the right hemisphere (96.49%) compared with the left (91.23%) (t(112)=--1.17, p=0.25). Its existence on one side was predictive at 91.07% of its presence on both sides. The SOS average location was y=62.35(±0.30), z=5.02(±0.67) on the left side and y=61.46(±0.37), z=7.28(±0.73) on the right side. The ASOS average location was

y=61.81(±0.28), z=-6.96(±0.56) on the left side and y=61.75(±0.31), z=-5.98(±0.52) on the right side.

The polar medial sulcus (PMS), found in 92.98% of the hemispheres, was not more present on one side compared to the other (left: 91.23%; right: 94.74%, t(112)=-0.73, p=0.47). Its existence on one side was predicted by its existence on the other side (85.96%). The PMS average location was y=65.61(±0.28), z=-0.51(±0.51) on the left side and y=65.40(±0.34), z=1.53(±0.66) on the right side.

Finally, we identified in some subjects a small sickle-shaped sulcus just dorsal to the olfactory sulcus. We labelled this unnamed sulcus the Ventro-Polar Sulcus (VMPS). It was only found in 39.47% of the hemispheres with a trend for a difference between the two hemispheres (left: 31.58%, right: 49,12%, left vs right: t(112)=-1.73, p=0.09). The probability of having this sulcus in the two hemispheres given its presence on one or the other side was 36.36%, suggesting that it is more common to have this sulcus on only one hemisphere. The VMPS average centre of gravity was y=58.34(±0.37), z=-16.42(±0.43) on the left side and y=58.84(±0.28), z=-17.29(±0.21) on the right side.

Description of patterns

We next examined the interactions between the different sulci. In agreement with Mackey and Petrides, (2014), several interaction patterns between the SU-ROS and other

224 sulci were identified. A fourth kind was also noted but it represented less than 5% of
225 our subjects. We subdivided each group based on the presence or absence of a PCGS.
226
227 Type 1 corresponds to a merging of the SU-ROS with the cingulate sulcus (sub-
228 type 1a) or with the paracingulate sulcus (sub-type 1b). In type 2, the SU-ROS merges
229 with one or several polar sulci but not with the cingulate or paracingulate sulci.
230 Subtypes were defined based on the polar sulcus with which the SU-ROS merges (2a:
231 SOS; 2b: ASOS; 2c: PMS; 2d: merges with several polar sulci). Type 3 refers to a merging
232 of the SU-ROS with both the cingulate sulcus and a polar/supra-orbital one. Similar to
233 subtypes identified in the type 2, subtype 3a merges with the cingulate sulcus while
234 subtype 3b merges with the paracingulate sulcus. These subtypes could also be
235 separated in groups according to which polar sulcus the SU-ROS merges with (3a1:
236 SOS, 3a2: ASOS, 3a3: PMS, 3a4: two polar sulci) (Figure 2A). The type 4 corresponds to a
237 merging with both cingulate and paracingulate sulci (subtype 4a). It could also merge
238 with polar sulci (subtype 4b) (Figure 2B).
239
240 In agreement with Mackey and Petrides (2014), we found that 19.3% of all
241 hemispheres belong to type 1, 17.5% to type 2, and 60.5% to type 3. Type 4 was the
242 smallest group with only 2.6% of hemispheres showing this pattern (Figure 2C & D).
243
244

245 ## Morphological deformation associated with sulcal pattern variability.

246 On the dorso-ventral axis, we observed that the barycentres of the ROS-S and
247 SU-ROS in the left hemisphere spread over 11 and 8mm, respectively (13 and 12mm in
248 the right hemisphere). In order to capture better how the inter-individual variability in
249 sulcal patterns impacts the organization of the vmPFC, we extracted for each subject the
250 antero-posterior and dorso-ventral MNI coordinates of the barycentre, the antero-dorsal
251 top extremity, the postero-ventral bottom extremity and the length of the ROS-S and the
252 SU-ROS. We computed the partial correlation coefficients between the 14 variables (Z
253 and Y MNI for barycentre, top extremity, bottom extremity and sulcal length for each
254 sulcus) and the following 6 factors: absence or presence of the SILS, ROS-I and PCGS
255 and the assignment to pattern 1, 2 or 3. Significant influences were observed related to
256 the presence of the SILS and ROS-I but not for the PCGS (all $p>0.05$). An effect of
257 patterns 2 and 3 were also observed but nothing for pattern 1 (all $p>0.05$) (Figure 3A).
258 We describe the significant results in the following part.

259

260 ### SILS

261 The presence of the SILS had a strong influence of the MNI location of the SU-
262 ROS because it induced a global mean shift of 3.1mm (MNI-space) of the SU-ROS
263 toward the antero-ventral direction. Indeed, the MNI Y and Z coordinates of the SU-
264 ROS were shifted for the barycentre (Y: shift=2.5mm, rho=0.35, $p=2.10^{-4}$; Z: shift=1.8mm,
265 rho=-0.21, p=0.03) and the top extremity (Y: rho=0.28, $p=3.10^{-3}$; Z: rho=-0.29, $p=2.10^{-3}$).

266 The bottom extremity was also shifted toward the anterior direction (Y: rho=0.30,
267 $p=1.10^{-3}$). Additionally, the ROS-S length was shorter when an SILS was present (rho=-
268 0.19, p=0.04) (Figure 3B).
269
270 ROS-I
271 We found that the presence of an ROS-I had a strong impact on the MNI location
272 of both principal sulci: ROS-I presence was dorsally shifting the barycentre of the ROS-S
273 (Z: shift=2.2mm, rho=0.39, $p=3.10^{-5}$) and the SU-ROS (Z: shift=2.7, rho=0.34, $p=3.10^{-4}$).
274 This dorsal shift could also be seen in a drift of the bottom and top extremities of both
275 sulci (Top SU-ROS: rho=0.24, p=0.01, ROS-S: rho=0.46, $p=4.10^{-7}$; Bottom SU-ROS:
276 rho=0.30, $p=2.10^{-3}$, ROS-S: rho=0.21, p=0.03). An additional effect of ROS-I presence was
277 found on the ROS-S length: it was longer in hemispheres with an ROS-I compared to
278 hemispheres without it (rho=0.29, $p=2.10^{-3}$). This was also observed in a significant effect
279 on the anterior location of the top extremity (rho=0.20, p=0.03) (Figure 3C).
280
281 As the presence or absence of ROS-I and SILS had opposite effects, we checked to
282 what extent a hemisphere with ROS-I but without SILS would have a shift in its ROS-S
283 and SU-ROS locations compared to a hemisphere without ROS-I but with SILS. The
284 average antero-ventral shift in MNI space was 3.5mm and 4.2mm for the ROS-S and the
285 SU-ROS, respectively. The maximal dorso-ventral distance observed between such two
286 opposite hemispheres was 16.3mm (9.3 mm for the antero-posterior direction). This
287 result shows that the deformations associated with sulcal morphology can be critical for

288 the interpretation of activity based solely on MNI coordinates compares to an
289 anatomical referential.
290
291 Patterns
292 We did not observe a significant effect of the PCGS on the ROS-S or the SU-ROS
293 morphology. Therefore, we merged the different subgroups of patterns based on the
294 presence or absence of a PCGS to test for an effect of patterns on ROS-S and SU-ROS
295 morphology. We only observed an effect on the SU-ROS antero-posterior location.
296 Indeed, the SU-ROS in pattern 2 was more anterior (Barycentre: shift=2.4mm, rho=0.24,
297 p=0.01; Top extremity: rho=0.23, p=0.02). The pattern 3 also induced an anterior shift of
298 the barycentre of the SU-ROS (shift=2.0mm, rho=0.23, p=0.02) (figure 3D).
299
300 To further characterize the feature that had the greatest influence on the sulcal
301 morphological variability in the vmPFC, we carried out a Principal Component
302 Analysis (PCA) on the 14 variables collected for every hemisphere. The first three
303 components explained 84.1% of the variance in the data (47.4%, 24.8% and 11.9% for the
304 first, second and third component). We extracted those three first components and ran
305 again the partial correlation analysis against the six features of interest. The results
306 demonstrated that the ROS-I was the only feature significantly affecting the first
307 component (rho=0.31, p=9.10-4), the SILS was the only feature affecting significantly the
308 second component (rho=-0.27, p=5.10-3). The third component was significantly affected
309 by the ROS-I presence (rho=0.29, p=2.10-3) but not by any other features (despite trends

310 for pattern 2 and pattern 3, with rho=0.18, p=0.058 and rho=0.17, p=0.077 respectively).
311 This result suggests that the ROS-I presence or absence can explain more than 59.3% of
312 the variability in the data compared to at least 24.8% for the SILS presence.
313

314 ### Peak of default mode network related to sulcus location

315 Finally we tested whether interindividual variability of the vmPFC sulcal pattern
316 could impact its functional organization. This analysis was based on resting state
317 functional MRI and more specifically a network associated with the vmPFC: the default
318 mode network (DMN). The DMN is a network mainly composed of the vmPFC, the
319 posterior cingulate cortex and the lateral parietal cortex (Raichle, 2015). It can be easily
320 identified during resting state MRI (rs-fMRI) by applying Independent Component
321 Analysis (ICA). In the HCP dataset used in the present study, for each subject, the ICA
322 component corresponding to the DMN was identified. We then obtained a brain map of
323 the DMN component weights per subject. An average of those weights is displayed in
324 Figure 4A.
325

326 First, we determined whether a vmPFC sulci-based ROIs would be relevant for
327 the rs-fMRI analysis. We extracted the curvature (depth of the sulcus and gyrus) within
328 a broad vmPFC mask (see methods). We found a strong negative correlation between
329 DMN weights and curvature across subjects (left: t(56)=-8.10, $p=5.10^{-11}$; right: t(56)=-8.54,
330 $p=1.10^{-11}$)(Figure 4B). Critically, this result indicates that the sulci within the vmPFC

331 contribute more to the Default Mode Network than the gyri. In other words, a lack of
332 correlation between a vmPFC sulcus-based ROI and DMN weights cannot be attributed
333 to a poor sulcal MRI signal as opposed the one recorded on the gyrus.
334
335 We then extracted the DMN weights from the principal medial sulci (SU-ROS
336 and ROS-S) and the ROS-I and tested for a difference between them. We found an effect
337 of sulcus in a one-way ANOVA ($F(2,297)=18.7$, $p=2.10^{-8}$). Pairwise comparisons
338 indicated that the ROS-S had significantly higher weights than the SU-ROS ($t(226)=5.1$,
339 $p=8.10^{-7}$) and than the ROS-I ($t(184)=4.9$, $p=2.10^{-6}$). No effect of side was observed (all
340 $p>0.05$). Thus, at the group level, the ROS-S was identified as a main hub of the vmPFC
341 for the Default Mode Network (Figure 4C).
342
343 Given that the ROS-I had a strong influence on the location of the ROS-S, we
344 checked the validity of the previous result with a complementary ANOVA analysis
345 including two factors: 'group' and 'sulcus'. The group factor was defined as subjects
346 with and without ROS-I (1/0) and sulcus was defined as ROS-S and ROS-I (1/2). Again,
347 we found a strong effect of sulcus ($F(1,183)=20.11$, $p=1.10^{-5}$) but no effect of group
348 ($F(1,183)=0.04$, $p=0.85$) (Figure 4D). This finding confirms the previous result showing
349 that the ROS-S is a critical hub of the DMN independently of the existence of the
350 secondary ROS-I sulcus.
351

352 Finally, we extracted the DMN weights within the ROS-S and sorted each vertex
353 according to the Y axis. Given that each ROS-S across hemispheres had a different
354 length, we normalized the length of the sorted vector to fit a 100 points vector. We then
355 merged all the normalized vectors in a single matrix and observed that the highest
356 DMN weights were located in the anterior part of the ROS-S, starting around 50% of the
357 ROS-S length (Figure 4E). A simple comparison between the first half of the sulcus and
358 the second half confirmed this observation ($t(113)=-8.13$, $p=6.10^{-13}$). A representative
359 hemisphere of this result is depicted in Figure 4F. Thus, we identified that the ROS-S,
360 and its anterior part in particular, is the hub of the vmPFC subcomponent of the DMN.
361
362 As we intend here to show that taking into account morphological features such
363 as sulcal location might help the investigation of specific functions of the vmPFC, we
364 tested whether using a region of interest defined according to sulcal morphology was
365 better than using a sphere around a specific MNI coordinate. We compared four ways
366 of selecting a region of interest (ROI). The first one is an *a priori* ROI defined according
367 to the peak of activity corresponding to the 'Default Mode Network' term search in
368 neurosynth.com (y=50, z=-10). We labelled it 'Neurosynth hub'. The second and the
369 third ones were defined from the average map of the Default Mode Network on the
370 dataset used in our study and depicted in Figure 4A. The second one corresponds to the
371 cluster found on the average maps and the third one corresponds to the 10 vertices with
372 the highest DMN weights in the group. This procedure would be classically labelled as
373 'double dipping' or 'circular inference' since it is a selection of region following a

positive result. It would bias the result in favour of a positive result. The fourth one is an anatomically based ROI: for each subject we extracted the DMN weights of the anterior part of the ROS-S. All four ROIs had significant DMN weights (all $p>0.05$). Not surprisingly, the '10 best peaks in group' ROI showed a significantly higher effect than the a priori 'Neurosynth hub' ($t(113)=2.34$, $p=0.02$). Interestingly we found that the anatomically defined ROI had a significantly higher effect than the three other ROIs (1: $t(113)=3.52$, $p=6.10^{-4}$; 2: $t(113)=2.74$, $p=7.10^{-4}$; 3: $t(113)=3.57$, $p=5.10^{-4}$) (Figure 5). This result shows that using the anterior part of the ROS-S as a region of interest is more efficient at the group level than using MNI coordinates based on the group result. Thus, even by positively biasing a selection of MNI coordinates, we showed that using anatomical milestone is providing stronger results than using MNI coordinates as a reference.

DISCUSSION

The present study examined the sulcal morphology of the vmPFC and its relation to functional organization as reflected in resting state connectivity. We established that the superior rostral sulcus (ROS-S) and the supra-rostral sulcus (SU-ROS) can be found in all hemispheres and can thus be considered as the two principal sulci of the vmPFC. Organised around these two principal sulci of the vmPFC, we identified the probability of the presence of the supplementary medial sulci, such as the inferior rostral (ROS-I), the subgenual intralimbic (SILS) and the polar/supra-orbital

394 sulci (MPS, VMPS, SOS, ASOS). We then demonstrated that the presence or absence of
395 three supplementary sulci, namely the SILS, the ROS-I and PCGS had a major impact on
396 the morphology of the vmPFC. First, the presence of a SILS induces an antero-ventral
397 shift in the location of the SU-ROS. Second, the presence of an ROS-I induces a dorsal
398 shift of both the ROS-S and the SU-ROS. Thirdly, the SU-ROS merges with the PCGS, or
399 with the CGS when the PCGS is not present, and this pattern has an impact on the
400 location of the SU-ROS, although the shifts associated with the presence of SILS and
401 ROS-I were greater than those induced by the presence of the PCGS.

402 The present results are consistent with those by Mackey and Petrides (2014) who
403 examined cadaver brains on a smaller pool of subjects (n=13). In our study, the supra-
404 rostral sulcus was observed in all hemispheres while they identified it in 91.3% of the
405 hemispheres. This difference can be explained by a quite rare yet observed merging
406 between the superior rostral sulcus and the supra-rostral sulcus. This merging can be
407 observed either on the whole length of both sulci, resulting in a long and deep principal
408 medial sulcus, or on a continuous merging between the antero-dorsal extremity of the
409 ROS-S and the ventro-posterior extremity of the SU-ROS, resulting in an extremely long
410 sulcus. Another noticeable difference is related to the SILS. We strictly used the SILS
411 label only when no gyrus could be observed between the sulcus and the corpus
412 callosum and we report a higher proportion of presence of SILS than they do (44%
413 against 30%). MPS, SOS and ASOS were observed in a high percentage of hemispheres
414 but we were able to identify an additional polar sulcus in 40% of the studied
415 hemispheres. We called this sickle-shaped sulcus, for which we found no description in

416 the literature, the VMPS. On average its barycentre coordinates were y=58, z=-16. It is
417 located just dorsal to the olfactory sulcus, and rostral to the ROS-I if an ROS-I is present.
418 Having determined the inter-individual variability in sulcal patterns and its
419 impact on the vmPFC morphology, we then assessed whether sulcal morphology could
420 influence the functional organization of the vmPFC and whether it could be used to
421 better characterize functional activity observed in the vmPFC. For this purpose, we
422 selected the Default Mode Network activation as a tool since the cluster of activity
423 observed at the group level is covering a large part of the vmPFC. An important finding
424 was the demonstration that the main hub of the Default Mode Network in the vmPFC is
425 located in the anterior part of the ROS-S, independently of the presence or absence of
426 the secondary medial sulcus ROS-I that our results showed to have a strong influence
427 on the ROS-S location. In other words, the vmPFC peak of the functional DMN network
428 was always located in the rostral ROS-S, although the location of the ROS-S in
429 stereotaxic MNI coordinates could vary depending on the presence or absence of the
430 ROS-I. Thus, importantly, we showed that the vmPFC peak of the Default Mode
431 Network is best defined by *an anatomical sulcal feature* rather than the MNI location of
432 the group cluster peak.
433 Previous studies had shown that the location of functional activity in fMRI can
434 often be predicted by the local morphology of the sulci in the frontal cortex (Amiez,
435 2006; Amiez et al., 2013; Amiez and Petrides, 2014; Li et al., 2015; Amiez and Petrides,
436 2018). Morphological features not only explain cross-subject variability in functional
437 connectivity but also explain behavioural measures (Bijsterbosch et al., 2018). However,

438 to the best of our knowledge, this is the first time that it is shown that the functional
439 organization of the vmPFC in resting state can be predicted by its local sulcal
440 morphology. It should be noted that Mackey and Petrides (2014) have examined the
441 sulcal patterns of the vmPFC in relation to cytoarchitecture and demonstrated that there
442 is a good relation between the sulci and particular cytoarchitectonic areas. Based on the
443 location of the DMN peak in the rostral part of the ROS-S, it is therefore likely that the
444 core node of the DMN in the medial prefrontal cortex is associated with a granular
445 cortex area 14m or area 10m (Bludau et al., 2014; Mackey and Petrides, 2014).
446 Supporting this anatomical correspondence between the vmPFC DMN node and area
447 10m is the fact that both have been functionally associated with supporting socio-
448 cognitive functions (Mars et al. 2012). Anterior cingulate cortex (ACC) contributions to
449 the DMN have also been often reported in the literature (Mantini et al., 2011; Qin and
450 Northoff, 2011; Vincent et al., 2007). However our results would suggest that the
451 implication of the ACC to the DMN is related to the strong monosynaptic connections
452 of cingulate 24 and 32 with the frontopolar cortex (Petrides and Pandya, 2007). Future
453 investigation should now be directed to extending this finding to other task-related
454 functional activity in other subdivisions of the vmPFC, such as in tasks examining
455 response to decision variables (Lopez-Persem et al., 2016) or subjective valuation
456 (Lebreton et al., 2009).

457 In conclusion, the present study provides a description of the variability of the
458 vmPFC sulcal morphology across individuals and demonstrates that this variability
459 might reduce the anatomical precision of the group-average analysis. Thus, taking into

account the local morphology of the vmPFC at the individual level to define regions of interest might be considered seriously when assessing the multiple functions of this heterogeneous brain region.

ACKNOWLEGEMENT

Data were provided by the Human Connectome Project, WU-Minn Consortium (Principal Investigators: David Van Essen and Kamil Ugurbil; 1U54MH091657) funded by the 16 NIH Institutes and Centers that support the NIH Blueprint for Neuroscience Research; and by the McDonnell Center for Systems Neuroscience at Washington University. ALP received a fellowship from the Fondation pour la Recherche Medicale. JS was supported by a Sir Henry Dale Wellcome Trust Fellowship (105651/Z/14/Z).

AUTHOR CONTRIBUTIONS

AL-P: Conceptualization, analysis and interpretation of data, writing and revising the article; LV: Methodology, interpretation of data, revising the article; CA: Conceptualization, revising the article; MP: Conceptualization, revising the article; JS: Supervision, conceptualization, interpretation of data, writing and revising the article.

BIBLIOGRAPHY

Amiez, C., 2006. Local Morphology Predicts Functional Organization of the Dorsal Premotor Region in the Human Brain. J. Neurosci. 26, 2724–2731. https://doi.org/10.1523/JNEUROSCI.4739-05.2006

Amiez, C., Neveu, R., Warrot, D., Petrides, M., Knoblauch, K., Procyk, E., 2013. The Location of Feedback-Related Activity in the Midcingulate Cortex Is Predicted by Local Morphology. J. Neurosci. 33, 2217–2228. https://doi.org/10.1523/JNEUROSCI.2779-12.2013

Amiez, C., Petrides, M., 2018. Functional rostro-caudal gradient in the human posterior lateral frontal cortex. Brain Struct. Funct. 223, 1487–1499. https://doi.org/10.1007/s00429-017-1567-z

Amiez, C., Petrides, M., 2014. Neuroimaging evidence of the anatomo-functional organization of the human cingulate motor areas. Cereb. Cortex 24, 563–578.

Bartra, O., McGuire, J.T., Kable, J.W., 2013. The valuation system: A coordinate-based meta-analysis of BOLD fMRI experiments examining neural correlates of subjective value. NeuroImage 76, 412–427. https://doi.org/10.1016/j.neuroimage.2013.02.063

Bijsterbosch, J.D., Woolrich, M.W., Glasser, M.F., Robinson, E.C., Beckmann, C.F., Van Essen, D.C., Harrison, S.J., Smith, S.M., 2018. The relationship between spatial configuration and functional connectivity of brain regions. eLife 7. https://doi.org/10.7554/eLife.32992

Bludau, S., Eickhoff, S.B., Mohlberg, H., Caspers, S., Laird, A.R., Fox, P.T., Schleicher, A., Zilles, K., Amunts, K., 2014. Cytoarchitecture, probability maps and functions of the human frontal pole. NeuroImage, In-vivo Brodmann Mapping of the Human Brain 93, 260–275. https://doi.org/10.1016/j.neuroimage.2013.05.052

Bonnici, H.M., Chadwick, M.J., Lutti, A., Hassabis, D., Weiskopf, N., Maguire, E.A., 2012. Detecting representations of recent and remote autobiographical memories in vmPFC and hippocampus. J. Neurosci. Off. J. Soc. Neurosci. 32, 16982–16991. https://doi.org/10.1523/JNEUROSCI.2475-12.2012

Chiavaras, M.M., Petrides, M., 2000. Orbitofrontal sulci of the human and macaque monkey brain. J. Comp. Neurol. 422, 35–54. https://doi.org/10.1002/(SICI)1096-9861(20000619)422:1<35::AID-CNE3>3.0.CO;2-E

Evans, A.C., Collins, D.L., Mills, S.R., Brown, E.D., Kelly, R.L., Peters, T.M., 1993. 3D statistical neuroanatomical models from 305 MRI volumes, in: 1993 IEEE Conference Record Nuclear Science Symposium and Medical Imaging Conference. Presented at the 1993 IEEE Conference Record Nuclear Science Symposium and Medical Imaging Conference, pp. 1813–1817 vol.3. https://doi.org/10.1109/NSSMIC.1993.373602

Fischl, B., 2012. FreeSurfer. NeuroImage 62, 774–781. https://doi.org/10.1016/j.neuroimage.2012.01.021

Glasser, M.F., Coalson, T.S., Robinson, E.C., Hacker, C.D., Harwell, J., Yacoub, E., Ugurbil, K., Andersson, J., Beckmann, C.F., Jenkinson, M., Smith, S.M., Van Essen, D.C., 2016. A multi-modal parcellation of human cerebral cortex. Nature 536, 171–178. https://doi.org/10.1038/nature18933

Glasser, M.F., Sotiropoulos, S.N., Wilson, J.A., Coalson, T.S., Fischl, B., Andersson, J.L., Xu, J., Jbabdi, S., Webster, M., Polimeni, J.R., Van Essen, D.C., Jenkinson, M., 2013. The minimal preprocessing pipelines for the Human Connectome Project. NeuroImage, Mapping the Connectome 80, 105–124. https://doi.org/10.1016/j.neuroimage.2013.04.127

Hänsel, A., von Känel, R., 2008. The ventro-medial prefrontal cortex: a major link between the autonomic nervous system, regulation of emotion, and stress reactivity? Biopsychosoc. Med. 2, 21. https://doi.org/10.1186/1751-0759-2-21

Jenkinson, M., Beckmann, C.F., Behrens, T.E.J., Woolrich, M.W., Smith, S.M., 2012. FSL. NeuroImage 62, 782–790. https://doi.org/10.1016/j.neuroimage.2011.09.015

Lebreton, M., Jorge, S., Michel, V., Thirion, B., Pessiglione, M., 2009. An Automatic Valuation System in the Human Brain: Evidence from Functional Neuroimaging. Neuron 64, 431–439. https://doi.org/10.1016/j.neuron.2009.09.040

Li, Y., Sescousse, G., Amiez, C., Dreher, J.-C., 2015. Local Morphology Predicts Functional Organization of Experienced Value Signals in the Human Orbitofrontal Cortex. J. Neurosci. 35, 1648–1658. https://doi.org/10.1523/JNEUROSCI.3058-14.2015

Lopez-Persem, A., Domenech, P., Pessiglione, M., 2016. How prior preferences determine decision-making frames and biases in the human brain. eLife 5, e20317.

Mackey, S., Petrides, M., 2014. Architecture and morphology of the human ventromedial prefrontal cortex. Eur. J. Neurosci. 40, 2777–2796. https://doi.org/10.1111/ejn.12654

Mantini, D., Gerits, A., Nelissen, K., Durand, J.-B., Joly, O., Simone, L., Sawamura, H., Wardak, C., Orban, G.A., Buckner, R.L., Vanduffel, W., 2011. Default Mode of Brain Function in Monkeys. J. Neurosci. 31, 12954–12962. https://doi.org/10.1523/JNEUROSCI.2318-11.2011

Marcus, D., Harwell, J., Olsen, T., Hodge, M., Glasser, M., Prior, F., Jenkinson, M., Laumann, T., Curtiss, S., Van Essen, D., 2011. Informatics and Data Mining Tools and Strategies for the Human Connectome Project. Front. Neuroinformatics 5. https://doi.org/10.3389/fninf.2011.00004

Marcus, D.S., Harms, M.P., Snyder, A.Z., Jenkinson, M., Wilson, J.A., Glasser, M.F., Barch, D.M., Archie, K.A., Burgess, G.C., Ramaratnam, M., Hodge, M., Horton, W., Herrick, R., Olsen,

T., McKay, M., House, M., Hileman, M., Reid, E., Harwell, J., Coalson, T., Schindler, J., Elam, J.S., Curtiss, S.W., Van Essen, D.C., 2013. Human Connectome Project informatics: Quality control, database services, and data visualization. NeuroImage 80, 202–219. https://doi.org/10.1016/j.neuroimage.2013.05.077

Noonan, M.P., Walton, M.E., Behrens, T.E.J., Sallet, J., Buckley, M.J., Rushworth, M.F.S., 2010. Separate value comparison and learning mechanisms in macaque medial and lateral orbitofrontal cortex. Proc. Natl. Acad. Sci. 107, 20547–20552. https://doi.org/10.1073/pnas.1012246107

Passingham, R.E., Stephan, K.E., Kötter, R., 2002. The anatomical basis of functional localization in the cortex. Nat. Rev. Neurosci. 3, 606–616. https://doi.org/10.1038/nrn893

Petrides, M., 2002. The Mid-ventrolateral Prefrontal Cortex and Active Mnemonic Retrieval. Neurobiol. Learn. Mem. 78, 528–538. https://doi.org/10.1006/nlme.2002.4107

Petrides, M., Baddeley, A., 1996. Specialized Systems for the Processing of Mnemonic Information within the Primate Frontal Cortex [and Discussion]. Philos. Trans. Biol. Sci. 351, 1455–1462.

Petrides, M., Pandya, D.N., 2007. Efferent Association Pathways from the Rostral Prefrontal Cortex in the Macaque Monkey. J. Neurosci. 27, 11573–11586. https://doi.org/10.1523/JNEUROSCI.2419-07.2007

Qin, P., Northoff, G., 2011. How is our self related to midline regions and the default-mode network? NeuroImage, Special Issue: Educational Neuroscience 57, 1221–1233. https://doi.org/10.1016/j.neuroimage.2011.05.028

Raichle, M.E., 2015. The Brain's Default Mode Network. Annu. Rev. Neurosci. 38, 433–447. https://doi.org/10.1146/annurev-neuro-071013-014030

Smith, S.M., Beckmann, C.F., Andersson, J., Auerbach, E.J., Bijsterbosch, J., Douaud, G., Duff, E., Feinberg, D.A., Griffanti, L., Harms, M.P., Kelly, M., Laumann, T., Miller, K.L., Moeller, S., Petersen, S., Power, J., Salimi-Khorshidi, G., Snyder, A.Z., Vu, A.T., Woolrich, M.W., Xu, J., Yacoub, E., Uğurbil, K., Van Essen, D.C., Glasser, M.F., 2013. Resting-state fMRI in the Human Connectome Project. NeuroImage, Mapping the Connectome 80, 144–168. https://doi.org/10.1016/j.neuroimage.2013.05.039

Uğurbil, K., Xu, J., Auerbach, E.J., Moeller, S., Vu, A.T., Duarte-Carvajalino, J.M., Lenglet, C., Wu, X., Schmitter, S., Van de Moortele, P.F., Strupp, J., Sapiro, G., De Martino, F., Wang, D., Harel, N., Garwood, M., Chen, L., Feinberg, D.A., Smith, S.M., Miller, K.L., Sotiropoulos, S.N., Jbabdi, S., Andersson, J.L.R., Behrens, T.E.J., Glasser, M.F., Van Essen, D.C., Yacoub, E., 2013. Pushing spatial and temporal resolution for functional and diffusion MRI in the Human Connectome Project. NeuroImage 80, 80–104. https://doi.org/10.1016/j.neuroimage.2013.05.012

Van Essen, D.C., Ugurbil, K., Auerbach, E., Barch, D., Behrens, T.E.J., Bucholz, R., Chang, A., Chen, L., Corbetta, M., Curtiss, S.W., Della Penna, S., Feinberg, D., Glasser, M.F., Harel, N., Heath, A.C., Larson-Prior, L., Marcus, D., Michalareas, G., Moeller, S., Oostenveld, R., Petersen, S.E., Prior, F., Schlaggar, B.L., Smith, S.M., Snyder, A.Z., Xu, J., Yacoub, E., WU-Minn HCP Consortium, 2012. The Human Connectome Project: a data acquisition perspective. NeuroImage 62, 2222–2231. https://doi.org/10.1016/j.neuroimage.2012.02.018

Vincent, J.L., Patel, G.H., Fox, M.D., Snyder, A.Z., Baker, J.T., Van Essen, D.C., Zempel, J.M., Snyder, L.H., Corbetta, M., Raichle, M.E., 2007. Intrinsic functional architecture in the anaesthetized monkey brain. Nature 447, 83–86. https://doi.org/10.1038/nature05758

Wallis, J.D., 2011. Cross-species studies of orbitofrontal cortex and value-based decision-making. Nat. Neurosci. 15, 13–19. https://doi.org/10.1038/nn.2956

592

593

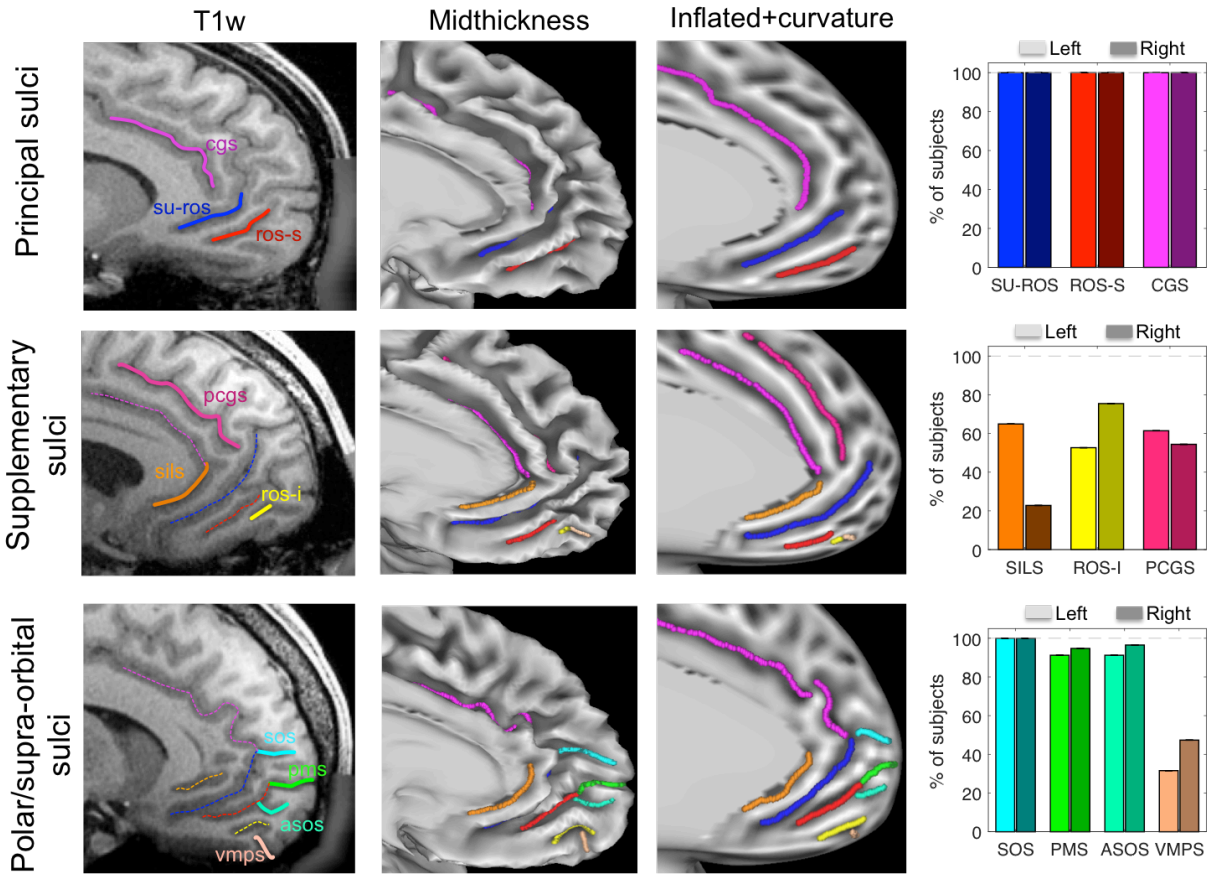

Figure 1: The ventromedial prefrontal cortex sulci

Sulci of the vmPFC were identified using three image renderings: T1 volumes (first column), midthickness surface (2nd column) and inflated surface with the curvature value (3rd column). First row: the two principal sulci: the supra-rostral sulcus (SU-ROS) and the superior rostral sulcus (ROS-S). Second row: The inferior rostral sulci (ROS-I) and the subgenual intralimbic sulcus (SILS) are supplementary sulci. Third row: The supra-orbital sulcus (SOS), the accessory supra-orbital sulcus (ASOS), the polar medial sulcus (PMS) and the ventro-polar sulcus (VMPS) composed the polar and supra-orbital sulci. Proportions of subjects with each sulcus are displayed in the fourth column for left (light colours) and right (dark colours) hemispheres. The cingulate sulcus (CGS) and the paracingulate sulcus (PCGS) are displayed for comparison purposes. Stars indicate significant differences between left and right hemispheres. On the volumes, solid lines represent the sulci of interest targeted in the fourth column. The dashed lines represent sulci identified in the preceding rows.

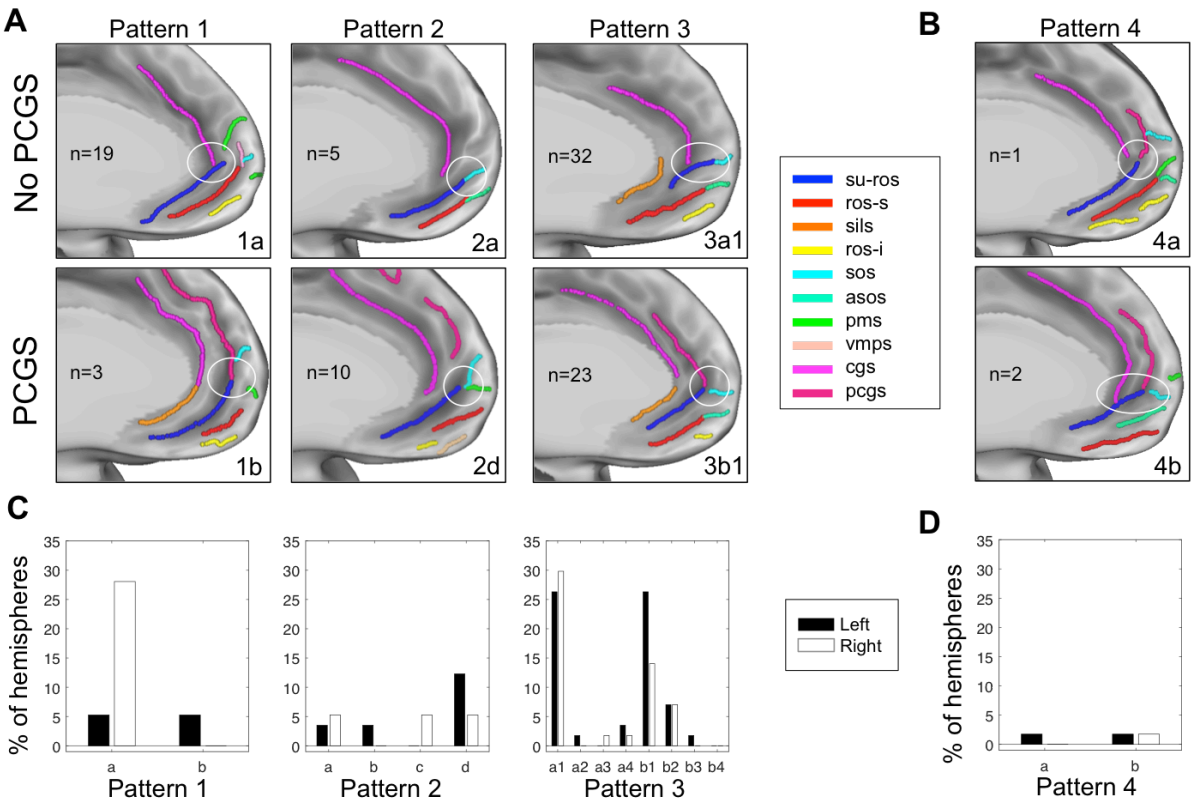

Figure 2: vmPFC anatomical patterns

A. Examples of the three common types of patterns in the vmPFC. Patterns depend on how the SU-ROS merges with other sulci (white circles) and the presence or absence of a paracingulate sulcus PCGS (second row) (first row). In type 1, the SU-ROS merges with either the CGS (top) or the PCGS (bottom). In type 2, the SU-ROS merges with one or more polar/supra-orbital sulci but not with the CGS (top) or the PCGS (bottom). In type 3, the SU-ROS merges with both polar/supra-orbital sulcus and CGS (top) or PCGS (bottom). B. In the rare type 4, the SU-ROS merges with both CGS and PCGS, without (top) or with (bottom) a merging with a polar/supra-orbital sulcus. n indicates the number of hemispheres with each pattern. C and D. Percentage of hemispheres on the left (black) and right (white) hemisphere for each pattern and sub-types of patterns. 1a: only CGS, 1b: only PCGS; 2a: only SOS, 2b: only ASOS, 2c: only PMS, 2d: two polar/supra-orbital sulci; 3a: with CGS or PCGS (3b) and SOS (3x1), or ASOS (3x2), or PMS (3x3) or two polar/supra-orbital sulci (3x4). 4a: CGS and PCGS; 4b: CGS, PCGS and polar/supra-orbital sulcus.

SU-ROS: Suprarostral sulcus; ROS-S: superior rostral sulcus; SILS: subgenual intralimbic sulcus; ROS-I: inferior rostral sulcus; SOS: supra-orbital sulcus, ASOS: accessory supra-orbital sulcus; PMS: polar medial sulcus; VMPS: ventro-polar sulcus; CGS: cingulate sulcus; PCGS: paracingulate sulcus.

595

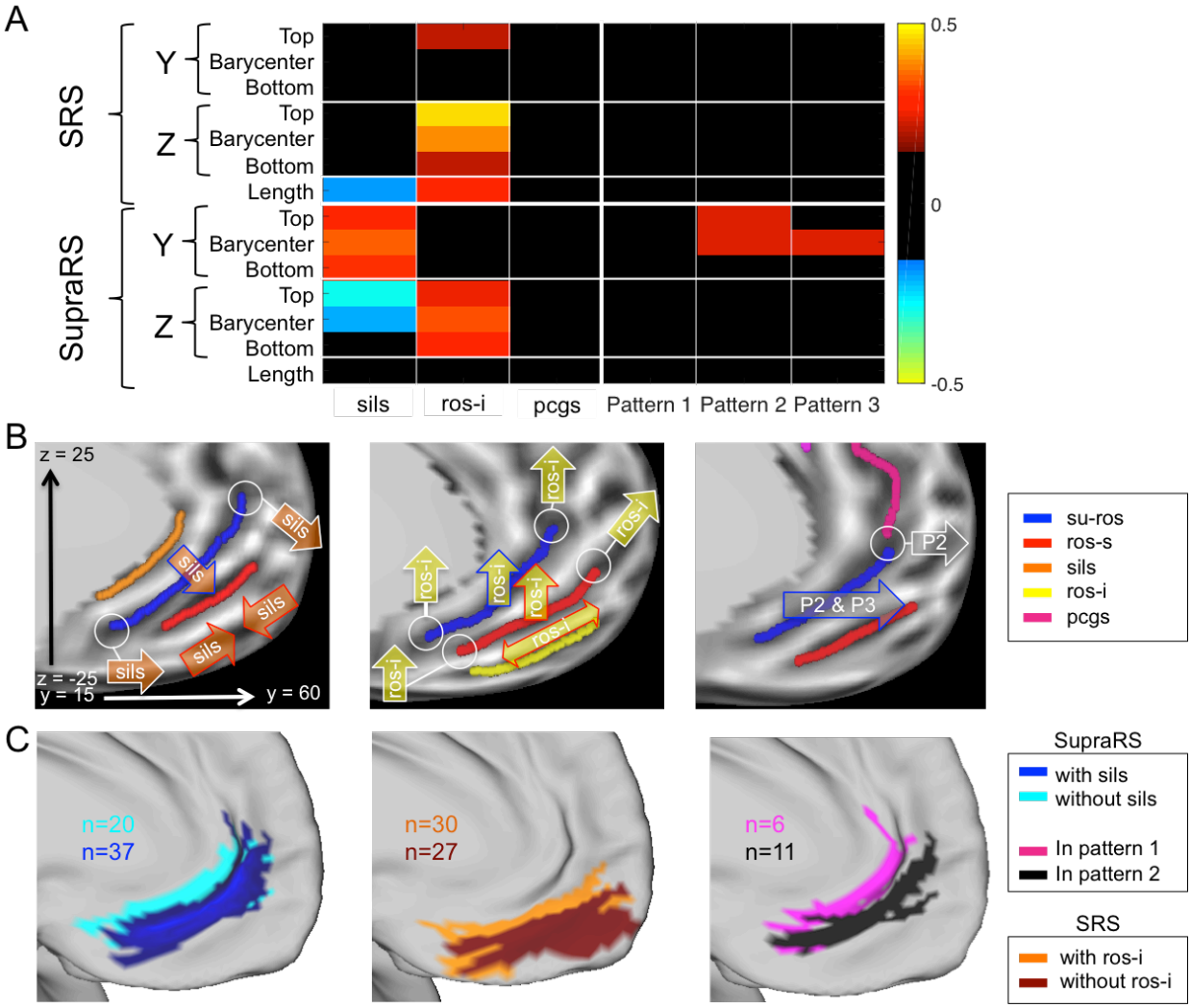

Figure 3: Morphological deformation associated with supplementary sulci presence and patterns

A. Partial correlation coefficients between each measure of interest of the ROS-S and SU-ROS and the presence of SILS, ROS-I, PCGS and patterns 1 to 3. Y and Z correspond to the antero-posterior and dorso-ventral coordinate respectively. 'Top' corresponds to the location of the most antero-dorsal extremity of each sulcus, 'Bottom' corresponds to the location of the most ventro-posterior extremity of each sulcus. 'Length' is the length of each sulcus. Only significant partial correlation coefficients are displayed ($p<0.05$). Hot colors indicate positive influence of having a supplementary sulcus or a specific pattern. Cold colors indicate negative effects. B. Schematic representation of the significant influence of the SILS presence (left), ROS-I presence (middle) and patterns 2 and 3 (P2 and P3, right) on the SU-ROS and ROS-S locations. Arrows attached to white circles indicate influence on circled extremity of the sulci; arrows with colored bordures indicate influence on the barycentres of the sulci; double arrows indicate a positive effect on length while two facing arrows indicate a negative effect on length. C. Left: Projection of all the left SU-ROS for subjects with and without SILS. Middle: Projection of all the left ROS-S for subjects with and without ROS-I. Right: Projection of all the left SU-ROS for subjects pattern 1 and subjects with pattern 2. n indicates the number of subjects displayed on the surface. SU-ROS: Suprarostral sulcus; ROS-S: superior rostral sulcus; SILS: subgenual intralimbic Sulcus; ROS-I: inferior rostral sulcus; PCGS: paracingulate Sulcus.

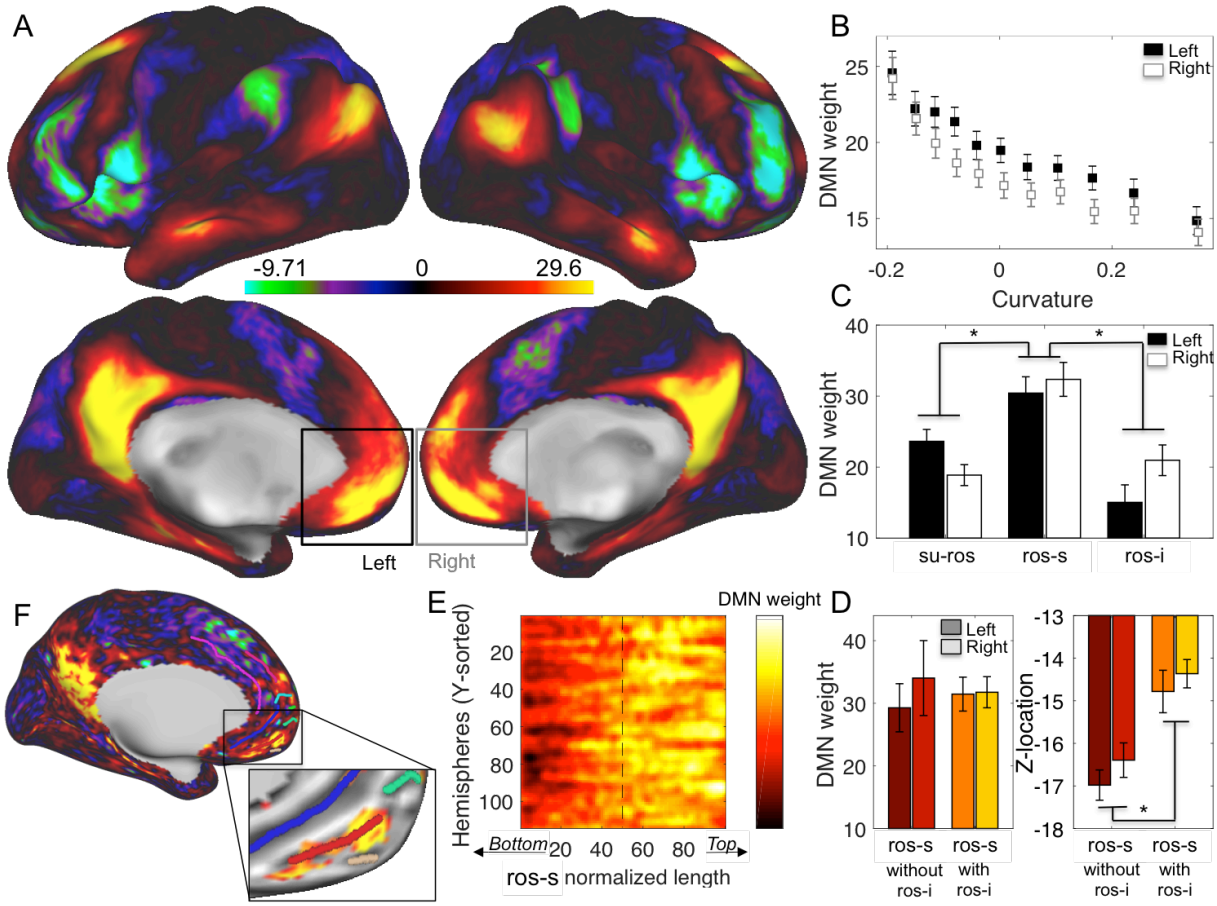

Figure 4: Default Mode Network weights and their dependence to the superior rostral sulcus.

A. Default Mode Network weights average across subjects on each hemisphere. B. DMN weights in function of bins of cortical curvature within the vmPFC for left (black) and right (white) sides. Positive curvature corresponds to gyri while negative curvature corresponds to sulci. C. Averaged DMN weights across subjects in the SU-ROS, the ROS-S and the ROS-I in left (black) and right (white) sides. D. Averaged DMN weights (left) and Z-MNI location (right) in the ROS-S across subjects without ROS-I (red) and with ROS-I (orange) for left (dark color) and right (light color). Error bars represent SEM. E. Matrix of all ROS-S aligned on their normalized length and sorted according to their Y-MNI location. Hot colors indicate high DMN weights. F. Subject example of DMN with sulci. Inset is a zoom of the vmPFC with an arbitrary threshold of the DMN weights. The strongest DMN weights are located on the anterior part of the ROS-S (red). SU-ROS: Suprarostral sulcus; ROS-S: superior rostral sulcus; ROS-I: inferior rostral sulcus.

597

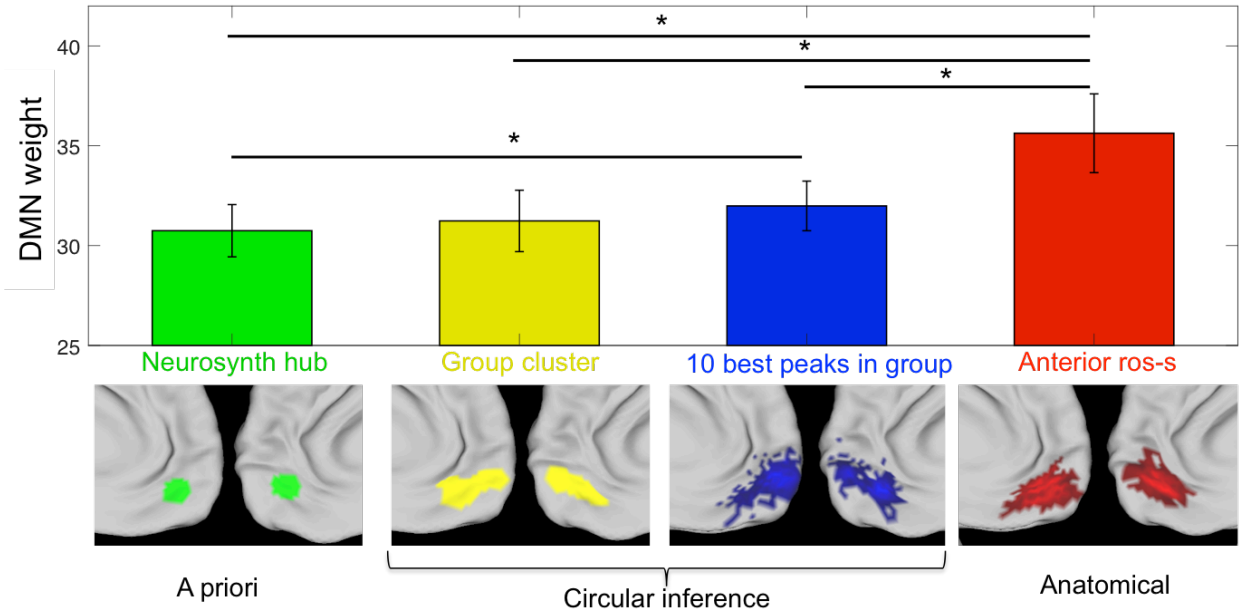

Figure 5: Default Mode Network weights in four vmPFC ROIs.

Default Mode Network weights average across subjects on each hemisphere for ROIs based on previous literature (neurosynth hub, green), on circular inference (yellow and blue) and on sulcal anatomy (red). Error bars represent SEM. ROIs overlap across subjects are represented on the second row. Stars indicate a significant difference.

598

Sulcus				ROS-I	ROS-S	SU-ROS	SILS	ASOS	SOS	VMPS	PMS	CGS	PCGS	PCGS-spur
MNI coordinates	barycenters	Left	X	-8.53	-7.15	-6.57	-4.26	-9.20	-9.26	-9.73	-10.55	-6.24	-7.02	-7.46
				0.12	*0.12*	*0.12*	*0.10*	*0.13*	*0.12*	*0.16*	*0.19*	*0.11*	*0.15*	*0.20*
			Y	54.60	48.20	44.86	39.09	61.81	62.35	58.34	65.61	33.71	46.52	53.13
				0.40	*0.61*	*0.42*	*0.45*	*0.28*	*0.30*	*0.37*	*0.28*	*0.61*	*0.94*	*0.71*
			Z	-17.18	-15.84	-8.78	-3.19	-6.96	5.02	-16.42	-0.51	27.89	27.15	22.26
				0.28	*0.34*	*0.46*	*0.82*	*0.56*	*0.67*	*0.43*	*0.51*	*0.50*	*1.06*	*1.16*
		Right	X	8.61	6.72	6.16	4.11	9.43	9.37	10.47	10.80	7.01	7.61	7.17
				0.17	*0.13*	*0.12*	*0.09*	*0.13*	*0.12*	*0.19*	*0.23*	*0.13*	*0.09*	*0.16*
			Y	54.67	46.68	44.37	38.34	61.75	61.46	58.84	65.40	31.15	47.23	49.02
				0.53	*0.49*	*0.37*	*0.38*	*0.31*	*0.37*	*0.28*	*0.34*	*0.80*	*0.95*	*1.07*
			Z	-17.23	-14.84	-6.45	-0.48	-5.98	7.28	-17.29	1.53	30.32	25.94	30.21
				0.26	*0.29*	*0.32*	*1.06*	*0.52*	*0.73*	*0.21*	*0.66*	*0.45*	*0.85*	*1.09*
	top extemity	Left	X	-9.48	-8.33	-8.50	-4.98	-10.18	-9.78	-9.62	-11.34	-5.94	-5.71	-6.21
				0.14	*0.14*	*0.13*	*0.15*	*0.16*	*0.15*	*0.21*	*0.24*	*0.15*	*0.11*	*0.27*
			Y	59.16	57.55	56.51	44.73	64.75	64.78	58.97	67.06	7.51	30.12	42.96
				0.27	*0.47*	*0.41*	*0.75*	*0.26*	*0.36*	*0.40*	*0.27*	*1.35*	*1.87*	*2.01*
			Z	-14.85	-11.39	0.21	4.74	-4.91	7.66	-15.37	1.29	47.55	45.78	35.89
				0.38	*0.60*	*0.67*	*0.99*	*0.61*	*0.69*	*0.46*	*0.53*	*0.70*	*1.28*	*2.05*
		Right	X	9.51	8.53	8.71	5.39	10.22	9.86	10.65	11.55	6.78	6.48	6.46
				0.19	*0.14*	*0.14*	*0.19*	*0.18*	*0.16*	*0.24*	*0.27*	*0.21*	*0.11*	*0.17*
			Y	58.87	58.14	54.77	43.00	64.12	64.04	59.86	67.09	2.43	29.86	34.37
				0.43	*0.34*	*0.49*	*0.98*	*0.35*	*0.41*	*0.30*	*0.28*	*1.81*	*2.16*	*2.08*
			Z	-14.92	-9.15	3.63	8.68	-4.22	9.52	-16.41	3.33	48.96	45.38	44.31
				0.36	*0.44*	*0.57*	*1.19*	*0.60*	*0.77*	*0.23*	*0.66*	*0.58*	*1.06*	*1.61*
	bottom extremity	Left	X	-7.80	-6.02	-4.78	-3.56	-8.41	-8.79	-9.22	-9.49	-6.61	-8.24	-8.43
				0.14	*0.15*	*0.12*	*0.10*	*0.12*	*0.11*	*0.18*	*0.16*	*0.19*	*0.18*	*0.16*
			Y	49.54	38.07	32.06	30.09	58.12	58.77	56.81	63.05	49.44	55.18	58.84
				0.68	*1.06*	*0.66*	*0.69*	*0.42*	*0.40*	*0.41*	*0.44*	*0.53*	*0.58*	*0.35*
			Z	-19.43	-19.05	-14.96	-8.71	-8.96	2.42	-17.07	-2.12	4.64	4.52	5.81
				0.24	*0.25*	*0.40*	*1.20*	*0.56*	*0.69*	*0.41*	*0.52*	*0.72*	*1.29*	*0.62*
		Right	X	7.76	5.18	3.89	2.85	8.59	9.01	9.79	9.64	7.53	8.70	8.37
				0.17	*0.14*	*0.12*	*0.10*	*0.13*	*0.12*	*0.19*	*0.20*	*0.19*	*0.11*	*0.16*
			Y	49.96	34.64	31.83	28.86	58.27	57.73	57.21	62.51	49.82	55.54	59.22
				0.78	*0.82*	*0.62*	*0.47*	*0.44*	*0.45*	*0.36*	*0.54*	*0.49*	*0.45*	*0.49*
			Z	-19.26	-18.80	-13.55	-6.26	-7.59	5.44	-18.01	0.12	6.01	2.93	12.88
				0.24	*0.28*	*0.36*	*1.54*	*0.51*	*0.74*	*0.21*	*0.73*	*0.58*	*0.66*	*1.22*
Characteristics (in mm, MNI space)	length	Left	mean	13.05	25.30	36.72	26.93	10.34	11.54	5.88	9.40	82.14	68.05	26.61
			SEM	*0.78*	*1.46*	*0.94*	*1.08*	*0.57*	*0.58*	*0.32*	*0.57*	*2.73*	*2.28*	*3.60*
		Right	mean	12.54	32.28	37.03	30.78	10.61	11.36	5.69	8.78	88.32	66.41	43.09
			SEM	*0.81*	*1.02*	*1.13*	*0.93*	*0.62*	*0.58*	*0.37*	*0.47*	*3.01*	*2.46*	*3.57*
	depth	Left	mean	-0.09	-0.13	-0.15	-0.07	-0.10	-0.12	-0.05	-0.09	-0.15	-0.14	-0.11
			SEM	*0.008*	*0.008*	*0.004*	*0.008*	*0.007*	*0.006*	*0.011*	*0.011*	*0.003*	*0.003*	*0.005*
		Right	mean	-0.10	-0.16	-0.14	-0.10	-0.11	-0.13	-0.06	-0.10	-0.14	-0.13	-0.09
			SEM	*0.007*	*0.004*	*0.003*	*0.005*	*0.008*	*0.005*	*0.011*	*0.009*	*0.003*	*0.003*	*0.004*
% of presence		Left		52.63	100	100	64.91	91.23	100	31.58	91.23	100	61.40	10.53
		Right		75.44	100	100	22.81	96.49	100	47.37	94.74	100	54.39	22.81
		All		64.04	100	100	43.86	93.86	100	39.47	92.98	100	57.89	16.67

Table 1: Summary description of the vmPFC sulci

Average (grey highlighted) and SEM (italic) MNI coordinates of the barycentre, top extremity and bottom extremity of each vmPFC sulcus on each hemisphere across subjects. Length, depth and percentage of presence are also reported. 'Top' corresponds to the location of the most antero-dorsal (postero-dorsal for cingulate sulci) extremity of each sulcus, 'Bottom' corresponds to the location of the most ventro-posterior (antero-ventral for cingulate sulci) extremity of each sulcus.

SU-ROS: Suprarostral sulcus; ROS-S: superior rostral sulcus; SILS: subgenual intralimbic sulcus; ROS-I: inferior rostral sulcus; SOS: supra-orbital sulcus, ASOS: accessory supra-orbital sulcus; PMS: polar medial sulcus; VMPS: ventro-polar sulcus; CGS: cingulate sulcus; PCGS: paracingulate sulcus; PCGS-spur: spur paracingulate sulcus